Surface imaging using total focusing method on surface waves for non destructive testing[1]

Mathieu Ducousso, [a,b] Olivier Ghibaudo[a], Stéphane Amiel[a]

[a] Safran Tech, Digital Sciences & Technologies Department, Rue des Jeunes Bois, Châteaufort, 78114 Magny-Les-Hameaux, France

[b] Laboratoire PIMM, Arts et Métiers Sciences et Technologies, CNRS, CNAM, HESAM Université, Paris, France

Corresponding author: mathieu.ducousso@safrangroup.com

Abstract

We demonstrate the effectiveness of total focusing methods (TFM) using Rayleigh waves for surface and sub-surface nondestructive inspection of different metals. The

[1] APPI Amplitude Phase Product Imaging
CFI Coherence Factor Imaging
ECT eddy currents
FMC full matrix capture
FWHM full width at half maximum
HFB hemispherical front bottom holes
IR thermography
MT magnetic particle testing
PA phased array
PCF Phase Coherence Factor
PCFI Phase Coherence Factor Imaging
PCI Phase Coherence Imaging
PT dye penetrant testing
PWI plane wave imaging
ROI region of interest
SAM scanning acoustic microscopy
SCF Sign Coherence Factor
SCFI Sign Coherence Factor Imaging
SSIM structural similarity index measure
TFM total focusing methods
Std Standard deviation

relatively low velocity of Rayleigh waves leads to sub-100 µm resolution imaging, with a penetration depth approximately equal to its wavelength. This allows for imaging and sizing sub-millimetric holes, possibly on coated material, as well as cracks, segregations, and other defects. The waves can propagate over long distances and works with curved surfaces or very close to edges. This shows potential for a new type of real-time surface inspection of large surfaces, with excellent spatial resolution. The process is free of chemical preparation and cleaning, and can be fully automated, from acquisition to decision or for making surface digital twin.

Keywords:

corrosion, cracks, ultrasonic imaging, Rayleigh wave, phased-array

1. Introduction

Surface inspection is used with almost all structural materials. In general, defects include cracks, porosities, discontinuities, leaks, laps, seams, inclusions, segregations, and so on. Because of their dimensions or their location just under the surface, indications may not be visible to the naked eye and so nondestructive methods have been developed to make these inspections. Classical methods are dye penetrant testing (PT) and magnetic particle testing (MT).

PT is the most widely used nondestructive testing method for detecting surface-breaking defects in various materials. It is relatively simple, cost-effective, and can be performed on a wide range of materials including metals, plastics, ceramics, and composites. However, it is important to note that PT is only a surface-level inspection method and can only detect defects that are open to the surface. It is not suitable for detecting internal flaws or defects that are covered by paint, coatings, or other surface treatments. Moreover, it suffers from some inherent drawbacks such as inspection being time-consuming, careful surface

preparation being required, and having a strong dependency on human factors. Finally, PT is a polluting technique that is under scrutiny by regulating agencies.

As an alternative method, MT is a nondestructive testing method used to detect surface and sub-surface defects in ferromagnetic materials. The principle behind MP is that when a magnetic field is applied to a ferromagnetic material, it creates lines of magnetic force within the material. If there is a defect or discontinuity on the surface or just below, these magnetic lines of force will be distorted or disrupted. The method is however limited to ferromagnetic materials and is sensitive to the alignment between the magnetic flux and the defect as well as the surface morphology. Resolutions are modest, in the mm range, [1] and post cleaning and post demagnetization are often necessary. Once again, the method has a strong dependency on human factors.

Alternative inspection methods are under development to avoid these limitations. These also need to be low cost, and have fast detection capabilities. Minimal ~~resolutions need~~resolution needs to ~~be at least similar to classical methods~~reach the sub-mm range. Moreover, several inspection configurations, in terms of materials, geometries, curvature, inspection zone, or accessibility must be possible.

Among the different possible methods, thermography (IR) and eddy currents (ECT) are interesting. In general, thermography relies on a surface temperature rise and on the space-time monitoring of the heat diffusion. In that way, thermography allows us to obtain an image of the heat diffusion at and under the surface of the structure under investigation. Currently multi-physical coupling, such as thermo-optical and thermo-magnetic approaches, are used to generate the temperature rise. For laser spot thermography, a continuous or pulsed laser is focused on the surface of the structure under inspection. The laser energy creates a local temperature rise and the spatio-temporal signature of the associated thermal flow allows

surface crack imaging. [2, 3, 4] One limitation of thermography is that the infrared emission also depends on the surface condition of the specimen (surface emissivity). However, the method depends on the surface optical accessibility and its morphology.

Eddy currents can also be used to perform surface and sub-surface inspections on conductive structures, e.g., for crack detection in metals. For internal defects, the eddy currents are different, resulting in a change of the induced magnetic field. Eddy current testing can only be performed on conductive materials and present some limitations, for example, it is sensitive to lift-off: i.e., the distance between the sensor and the surface, which can mask a defect. Lift-off is known to be one of the main obstacles for effective eddy current technology. A combination of the two techniques mentioned above can also be done. [5] However, such inspections combine the limitations of both methods.

Ultrasonic inspection is another type of inspection method, based on wave/matter interaction. Currently, ultrasound is mainly used to inspect the bulk of components or to evaluate material properties. The main advantages of ultrasound are the sensitivity, the ability to inspect thick and opaque materials, the possible automation of testing, and data recording. Moreover, PA probes, made up of numerous small ultrasound transducers, revolutionized ultrasound inspection 20 years ago, [6] improving productivity (compared to monolithic transducer) thanks to their large dimensions. Moreover, PA introduces the possibility to electronically deflect and/or focus the acoustic energy of bulk waves by applying time delays to the elements of the probe before summing the contribution of all the elements. They can be also used to generate and detect guided waves, [7] making nondestructive control applications possible. [8]

The TFM is the realization of such electronic delays and the summed use of PA: it allows us to focus the ultrasound beam at every point of a region of interest (ROI). It is considered

by some as the “gold standard” of ultrasound imaging. [9] It can be used with various acquisition schemes, such as FMC or PWI. [10] The FMC involves firing each array element individually with all the elements used to record the response of the structure, while in PWI all array elements are fired with appropriate time delays to generate sequences of different plane incident waves. The calculated image using TFM is called a T-scan.

Moreover, depending on the configuration, the nature of the inspected material, and the type of indication under investigation, different algorithms can be used to synthetize the image by performing the summation on the amplitude or on the phase of the signal. [9, 10, 11, 12, 13]

The TFM technique has been extended very recently to Rayleigh waves. [14] Such waves can be used in an NDT procedure to detect surface and sub-surface indications. They show high sensitivity and propagate over long distances since their energy is confined to the surface. By applying TFM to Rayleigh waves, complex surface cracks, extending over 18 mm, composed of several sub-cracks (from hundreds of microns to few millimeters), and with a crack opening of a few dozen microns on metallic parts have been characterized precisely. Additionally, such characterization has been done in real time at 27 Hz.

Following this first demonstration, we demonstrate here that Rayleigh waves combined with TFM imaging is a versatile tool for NDT. First, we will focus on the work in the image formation. In this part, we will analyze the image synthesis using different acquisition schemes and algorithms to calculate the images. Second, we will demonstrate the suitability of the method for different type of defects, such as cracks, corrosion pitting-like defects (hemispherical bottom hole, HFB), and freckle inclusion. Finally, we will focus on the complexity of the environment, demonstrating the performance of the method even if the indication is located under a few tens of µm coating, close (few tens of µm) to a sharp edge,

in a circular edge, after a sharp edge, or at the surface of a tube. Based on all of this, this work demonstrates a new type of real-time surface and sub-surface inspection, applicable to large and complex surfaces or for areas with difficult access. Furthermore, the method is free of chemical preparation and cleaning, and can be fully automated from acquisition to decision, making this form of inspection compatible with Industry 4.0 or digital twinning.

2. TFM and Rayleigh waves

2.1 Experimental configuration

The experimental configuration shown in Fig. 1 is similar to the one presented in the previous communication. [14]

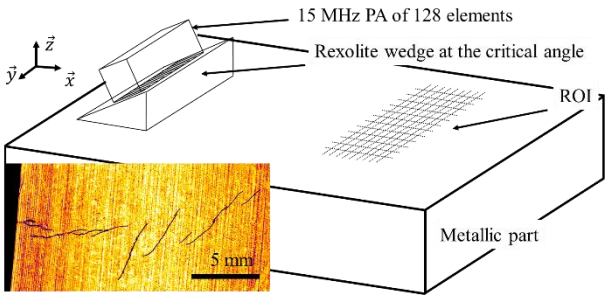

FIG 1. Schematic of the experiments. PA is fixed on a rexolite wedge at the critical angle in front of the surface cracks. Insert: Rayleigh wave microscopy (75 MHz) image of the cracks with an assume spatial resolution of 4 µm.

The sample is a plane monolithic metallic part. Imaging of its surface is realized using a PA probe composed of N = 128 elements, with a pitch of 0.15 mm and a dimension along the passive plane of 5 mm. The pitch of 0.15 mm allows us to minimize grating lobes and is a good compromise between manufacturing capabilities and the required sensitivity. Central frequency of the PA is 15 MHz, with a bandwidth of 70% at -6 dB. All the experimental results presented in this work were obtained with this probe.

The PA is coupled (ultrasonic coupling agent) to a rexolite wedge. Angle θ^w of the wedge has been defined to maximize the Rayleigh wave generation in the sample. It is simply defined by the following relationship:

$$\theta^w = asin\left(\frac{c_L^w}{c_R^s}\right), \quad (1)$$

were c_L^w define the longitudinal wave velocity in the wedge, and c_R^s define the Rayleigh wave velocity in the sample. It was measured at 2350 m·s^{-1} and 2970 m.s^{-1}, respectively. This leads to a wedge angle of 52°. The wedge was also designed to minimize the distance between the front of the wedge and the exit point of the acoustic field to generate surface waves of large amplitude at the surface of the sample.

Note that all the experiments presented in this work will be performed using the same PA and the same wedge (excepted for Section 4.4 which required a curved wedge but using the same angle). Experiments will however be done on different materials, such as steel, nickel-based alloy, and aluminum (experiments have also been performed on Ti6Al4V with same setup but are not shown here). This means that 1) the Rayleigh wave velocity does not change significantly between the different materials, which makes the control simpler from an experimental point of view; 2) the demonstration performed in this work is general and does not depend on the nature of the (metallic) material. Such point fits well with industrial confidentiality considerations and details on the materials will not be given in the following.

Finally, the PA orientation, parallel to the surface plane, allows imaging of the surface with Rayleigh waves using recent developments in ultrasonic imaging applying TFM. Such developments concern the acquisition schemes and the algorithms used to synthetize images. For each control, we performed FMC and PWI acquisitions. FMC involves the activation of each element one-by-one, while each element of the array is used as a receiver for each sequence. The PWI scheme considers plane waves emitted using all the PA elements at

different angles from Θ_1° to Θ_2° by using an electronic time delay between each element. The back-scattered signals are then recorded with all the elements without introducing delays at reception. In this work, we will systematically use 20 different angles, from −20° to +20° for the PWI acquisition scheme. Such a choice is arbitral, and have been done from real time visualization of the cracks presented on Fig. 1. It appeared as a good compromise between the amount of data and the expected sensitivity to image all the cracks.

2.2 Imaging algorithm

The imaging algorithms are tested on a sample presenting multiple cracks along its surface. The surface damage extends over 18 mm and is composed of several sub-cracks, from hundreds of microns to a few millimeters, and the crack opening is a few dozen microns. An image of the cracks, obtained from Rayleigh wave SAM at 75 MHz, is presented in the insert of Fig. FIG 1. Spatial resolution of the SAM image is 4 µm. Such image is considered as the reference and the different synthetized images from total focusing methods will be confronted to such reference. The depths of these cracks have been estimated to be around 1 mm. [14] Such a sample is interesting for that work because of the large damage surface area, but also because of the fine sub-structures and the different orientations in the damage. The SAM image also shows that, whatever the direction of propagation of the ultrasound, some of the sub-cracks will always be masked behind others. It has been previously used to present the method.

The PA driver used in this study is a Panther (Eddyfi Technologies, Les Ulis, France). The cracks are placed in front of the PA, which is placed on the rexolite wedge described above, a few cm from the cracks. The PA is not moved between the TFM and the PWI acquisitions. The dataset related to these two schemes is then used to synthesize ultrasound images focused on all points (TFM) in a ROI containing cracks.

Different algorithms, provided in the CIVA 2023 analysis package software, are used [15] to evaluate their performance in Rayleigh wave total focusing imaging. CIVA is a nondestructive testing software developed at CEA (French Atomic Energy Commission), commonly used for NDT simulation and data analysis.

The different algorithms evaluated are named Classical (Classical), Coherence Factor Imaging (CFI), Sign Coherence Factor Imaging (SCFI), Phase Coherence Factor Imaging (PCFI), and Phase Coherence Imaging (PCI). [7, 9, 10, 8] A review of phase coherent imaging have been recently proposed by Camacho et al. [16] Each algorithm can be used with a TFM or PWI acquisitions sequence. Let's quickly detail them:

Considering a FMC sequence, the intensity of the classical TFM image at pixel p is obtained by summing all received signals shifted in time:

$$I_{classical}(p) = \sum_{i,j=1}^{N} s_{ij}\left(t_{ij}(p)\right), \quad (2)$$

where $s_{ij}(t)$ is the signal received by element j when emitting with element i, $t_{ij}(p)$ is the corresponding time of flight, N is the number of elements of the array. The PCI algorithm uses only the phase terms in the summation process :

$$I_{PCI}(p) = \sum_{ij=1}^{N} \sin\left(\phi_{ij}\left(t_{ij}(p)\right)\right), \quad (3)$$

where $\phi_{ij}(t) = \tan^{-1}\frac{H(s_{ij}(t))}{s_{ij}(t)}$ is the phase of the received signal $s_{ij}(t)$ and H is the Hilbert transform operator. When using the CF algorithm, the output image is obtained by multiplication of classical TFM image by corresponding coherence factor *CF(p)*:

$$I_{CF}(p) = CF(p) \times I_{TFM}(p), \quad (4)$$

where $CF(p)$ is obtained by the following relation :

$$CF(p) = \left(\frac{\left(\sum_{ij=1}^{N} s_{ij}\left(t_{ij}(p)\right)\right)^2}{N^2 \sum_{ij=1}^{N}\left(s_{ij}\left(t_{ij}(p)\right)\right)^2} \right)^{cfSensitivity}. \quad (5)$$

The parameter $cfSensitivity$ is the CF sensitivity and have been empirically evaluated at 0.6 in that work. For SCFI, we first evaluate the SCF by considering the following formula:

$$SCF(p) = \left| 1 - \sqrt{1 - \left[\frac{1}{N^2}\sum_{ij=1}^{N} \text{sign}\left[s_{ij}\left(t_{ij}(p)\right)\right]\right]^2} \right|^{cfSensitivity}. \quad (7)$$

The SCFI image is then calculated by multiplication of the classical TFM image by SCF factor as:

$$I_{SCFI}(p) = SCF(p) \times I_{classical}(p), \quad (8)$$

Note that SCFI only requires processing one bit per channel (the sign), significantly reducing the amount of data, which is interesting for real-time operation at high frame rates.

Finally, the intensity of the PCF at pixel p is calculated by the following formula:

$$PCF(p) = \begin{cases} 1 - \frac{\sigma(p) \cdot cfSensitivity}{\sigma_0}, & \text{if } \frac{\sigma(p) \cdot cfSensitivity}{\sigma_0} < 1 \\ 0, & \text{otherwise} \end{cases}, \quad (9)$$

where $\sigma_0 = \frac{\pi}{\sqrt{3}}$ is the standard deviation of a random phase distribution between $-\pi$ and π and the term $\sigma(p)$ is an estimate of the phase diversity calculated from the phase standard deviation by:

$$\sigma^2(p) = \frac{1}{n}\sum_{i=1}^{n} \varphi_{ij}^2(p) - \left[\frac{1}{n}\sum_{i=1}^{n} \varphi_{ij}(p)\right]^2. \quad (10)$$

In the above formula, the phase, $\varphi_{ij}(p)$, of the received signal $s_{ij}(t)$ is given by:

$$\varphi_{ij}(p) = \tan^{-1} \frac{H\left(s_{ij}(p)\right)}{s_{ij}(p)}, \quad (11)$$

As in the previous two cases, the output image is obtained by multiplication of the classical TFM image by corresponding PCF factor:

$$I_{PCF}(p) = PCF(p) \times I_{TFM}(p), \quad (12)$$

Note that phase-based algorithms are not sensitive to the amplitude of the signal: attenuation of the signal or amplitude of the diffracted signal from a defect cannot be considered. One way to benefit from the advantages of both amplitude- and phase-based algorithms is to combine them by multiplying images obtained from both classical and phase coherent algorithms (APPI, for Amplitude Phase Product Imaging) :

$I_{APPI}(p) = I_{PCI}(p) \times I_{TFM}(p).$	*(13)*

Results are presented on Figs FIG 2 and IG 3. Amplitude of the signal is in dB with a reference defined by the maximal amplitude of the detected signal. The FMC sequence is used for Figure FIG 2, while the PWI sequence is used for Figure IG 3. For the sake of simplicity, each combination will be defined as sequence/algorithm, for example FMC/PCI stands for the use of a FMC sequence and PCI algorithm, while PWI/Classical stand for a PWI sequence and Classical algorithm. The PA array was fixed at the sample surface between the FMC and the PWI acquisition sequences in order to be able to compare the two different acquisition schemes.

First, from general comparison between Figures 2 and 3, the PWI sequence seems to generate a better SNR than the FMC sequence. We do not have for now a definitive explanation on it as a quantitative investigation on such point is out of the scope of this work but difference is probably more related on imaging artefacts than on structural noise from back-scattered signals (which should not change as function of the acquisition sequence). In that way, using filters, such as angular filters, could help to improve the SNR of images generated from FMC sequences. Similarly, the optimal configuration for that sample using PWI sequence could be defined from a detailed investigation on the number and amplitude of angles.

Moreover, as PWI requires less ultrasound emissions than FMC, repetition rate using PWI can be larger than using FMC, with smaller data files. Nevertheless, the actual reference sequence for TFM imaging is FMC. Finally, we decided to propose the comparison by

alternately using FMC or PWI in this article, and the complementary one will be systematically presented in the supplemental part of the article.

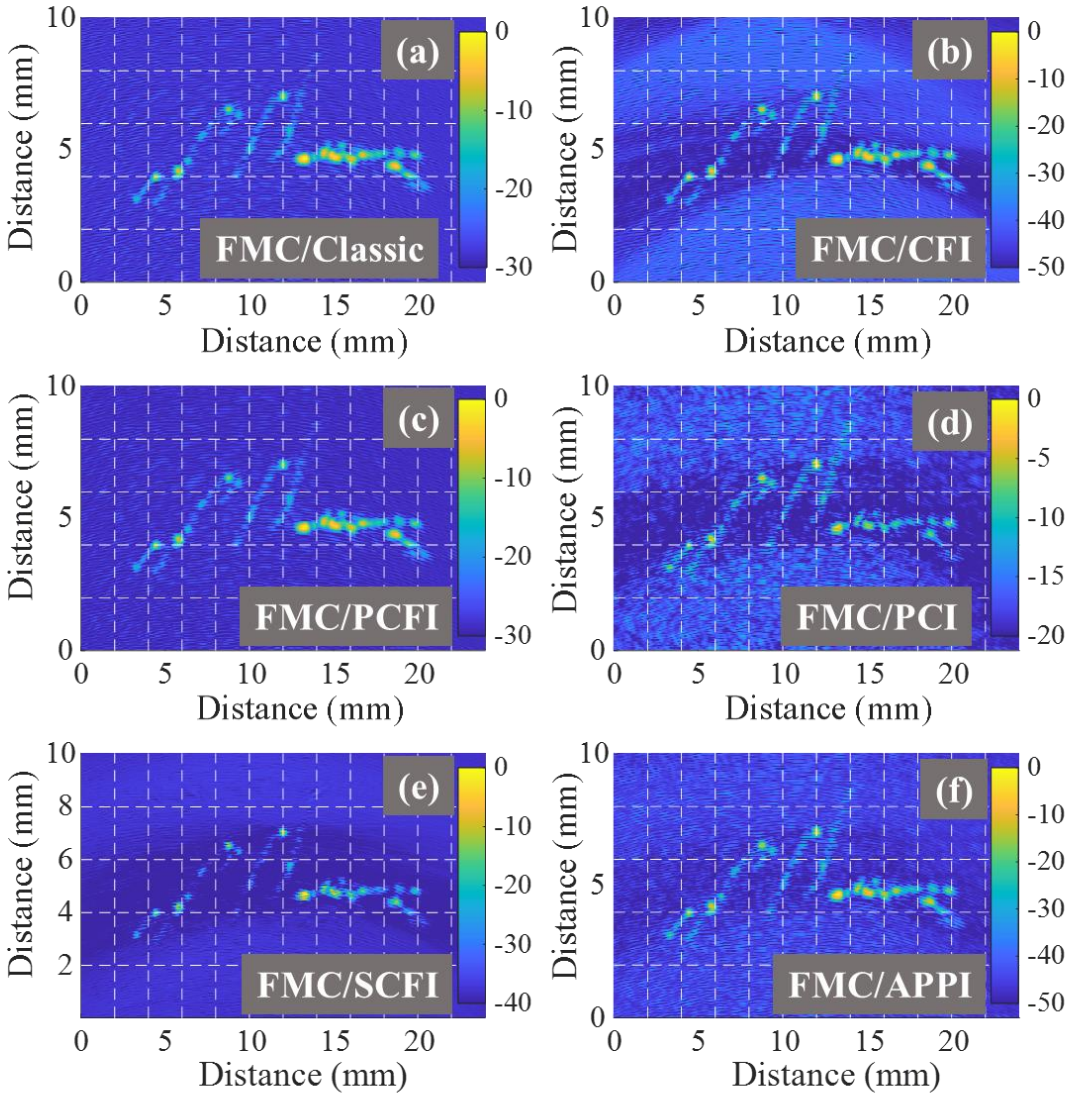

FIG 2. Total focusing imaging using Rayleigh waves of a large and complex crack using FMC sequence and different algorithms (Classic, CFI, PCFI, PCI, SCFI, and APPI). Acronyms of the algorithms are detailed in the text. Images are in dB scale.

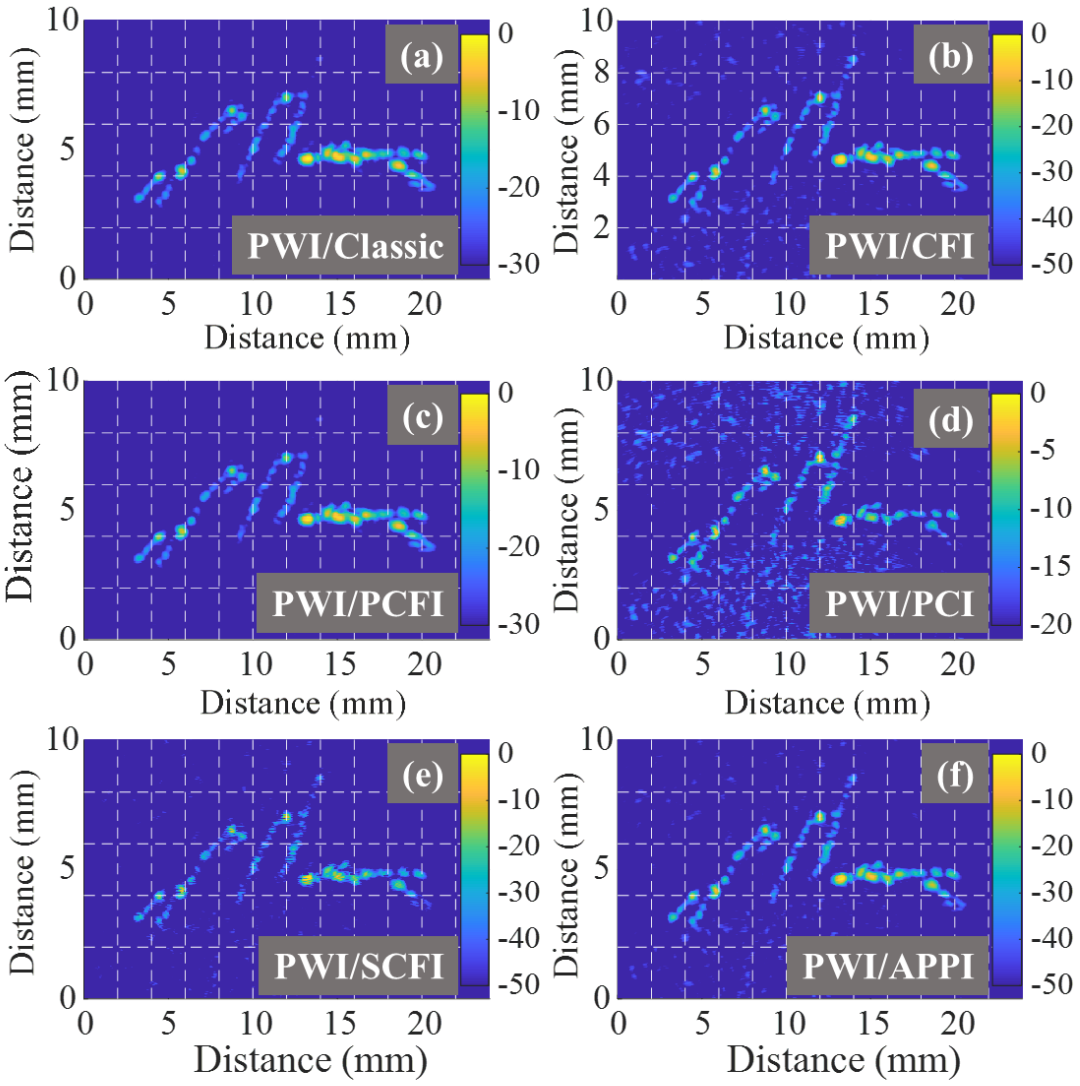

FIG 3. Total focusing imaging using Rayleigh waves of a large and complex crack using PWI sequence and different algorithms (Classic, CFI, PCFI, PCI, SCFI, and APPI). Acronyms of the algorithms are detailed in the text. Images are in dB scale.

Next, we compare the use of the different algorithms for imaging the cracks. From a naked eye qualitative analysis, classical algorithm allows imaging almost all the cracks with significant signal while; by comparison, phased-based algorithms are less reproducible, as different behaviors arise depending on the algorithm. For instance, some of the long parts of cracks are almost undetectable using CFI and SCFI, especially using a FMC sequence. Such

point is not surprising as phase based algorithms are known to be more sensitive for detection on diffraction echoes instead of specular ones. [16] In the same way, some artifacts appear using CFI and PCI algorithms.

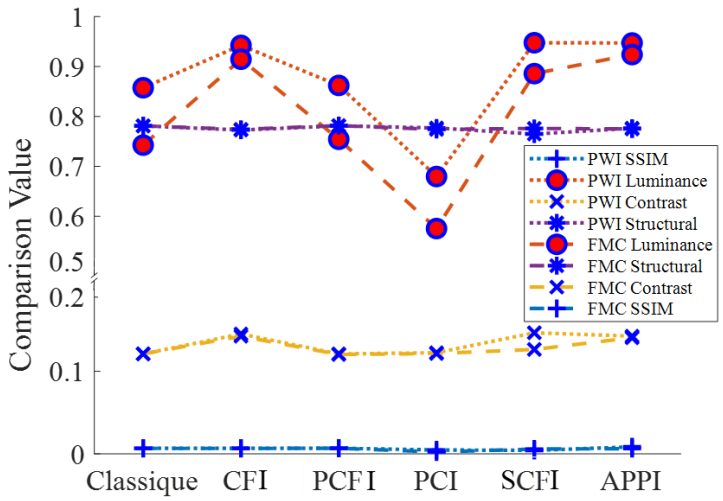

FIG 4. Evaluation of the luminance, the contrast and the structure of each image generated by the different experimental sequences and algorithms with comparison to the SAM image.

A qualitative evaluation of the use of the algorithms for imaging the cracks is attempted by considering SSIM. [17] SSIM have found strong adoption in the image processing community and some applications in NDT. [8] It allows to propose a quantitative comparison between the synthetized images with a reference one. Comparison is done here on the smallest image as possible but which encompass the whole cracks in order to have the larger dynamics as possible; defined by $3 < x < 18$ and $2.5 < y < 7.5$.

We considered here the SAM image presented on Fig. 1 as the reference. The SSIM is based on three different evaluations, between the sample and the reference: a luminance comparison $l(x,y)$; a contrast comparison $c(x,y)$ and a structure comparison. SSIM is then defined as the

product of the three comparisons. [17] Considering an image *x* of *N* pixel, its mean intensity is defined as $\mu_x = {}^1\!/_N \sum_{i=1}^N x_i$ and

$$l(x,y) = \frac{2\mu_x\mu_y + C_1}{\mu_x^2 + \mu_y^2 + C_1}, \tag{14}$$

where C_1 is a constant used to avoid instability. Similarly, defining the standard deviation of the image as $\sigma_x = \sqrt{{}^1\!/_{(N-1)} \sum_{i=1}^N (x_i - \mu_i)^2}$, the contrast comparison function takes a similar form :

$$c(x,y) = \frac{2\sigma_x\sigma_y + C_2}{\sigma_x^2 + \sigma_y^2 + C_2}, \tag{15}$$

where C_2 is another constant, also used to avoid instability. Structure comparison is defined as :

$$s(x,y) = \frac{\sigma_{xy} + C_3}{\sigma_x\sigma_y + C_3}, \tag{16}$$

where $\sigma_{xy} = {}^1\!/_{(N-1)} \sum_{i=1}^N (x_i - \mu_x)(y_i - \mu_y)$ and C_3 is a constant. Finally, SSIM is defined as :

$$SSIM(x,y) = [l(x,y)]^\alpha [c(x,y)]^\beta [s(x,y)]^\gamma, \tag{17}$$

where α, β and γ are positive constants used to adjust the relative importance of the three components. Results of the 4 calculations (l(x,y), s(x,y), c(x,y) and SSIM, with α=β=γ=1) are presented on fig. 4. Note that the *y* axis have been break between 0.2 and 0.5 in order to better visualize the respective dynamics (values are presented in supplemental material) of the parameters.

SSIM is the product of three low value parameters and does not seem pertinent to analyse in comparison to the three others. First, results are almost not depending on the FMC or PWI choice, expected for the luminance, which is higher for PWI-based images than for the FMC ones. As luminance is related to the intensity of the image, such results is not surprising.

Moreover, luminance is sensitive to both indication and noise, as highest luminance values are founded for images with significant background noise (CFI, PCI, SCFI, APPI).

Contrast and structure are more interesting for evaluating the synthetized image. They seems to have correlated behavior, as a (relative) high value of contrast correspond to a (relative) low structure value and vice-versa. As structure parameter allows quantifying the crack pattern imaging (with respect to the SAM reference), we are finally focused on it only and, similarly to the naked eye observation, classical and PCFI algorithms seems to be the best one.

Finally, classical algorithm remain a reference algorithm, even for Rayleigh wave imaging. However, in some cases, phase-based algorithms, such as PCFI, are nevertheless very effective. In the following section, all the experiments have been imaged by using the FMC and the PWI sequences, leading to similar results. And, for sake of simplicity, we will present results synthetized using only the Classical algorithm even if other algorithms can also be used with similar results.

3. Imaging of different surface indications

3.1 Reference crack imaging

The crack imaging capability using this approach has been demonstrated previously. Here we investigate the sizing capacity of the method by comparisons between references images and ultrasonic images on simple, linear cracks at the surface of plane metallic sample. An illustration of such a type of crack is presented on Fig. 5. We used a PWI sequence (the image obtained using the FMC sequence is in the supplementary material). The two images compare well in terms of morphology and size at the same scale. Such comparative work was performed on five different cracks on nickel-based material.

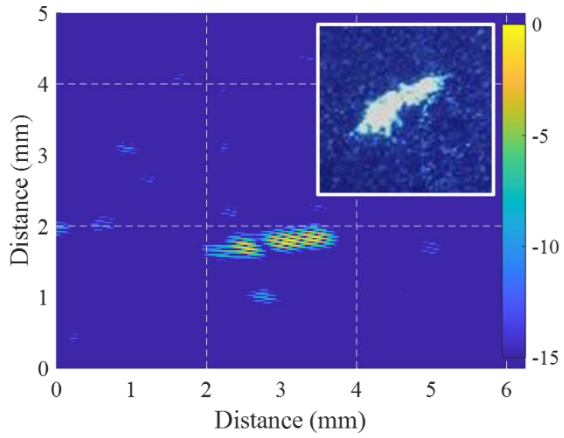

FIG 5. PWI acquisition. Illustration of the comparison of images obtained on a linear crack from ultrasonic and visualization after PT (insert). A similar sizing is obtained. UT image is in dB scale.

The results are synthetized in Table **Erreur ! Source du renvoi introuvable.**. The cracks have been characterized by length and size of surface opening from microscopy inspection. Length evaluation was performed from small magnification observation (×20) after PT application and cleaning. The opening size was measured from a large magnification observation using white light. The crack's opening can be as small as 2 µm. We also present the length UT sizing. We found a good agreement between the two evaluations, even if UT sizing seems to downsize the crack's length, maybe because of an opening under the ultrasonic amplitude at the crack's extremity.

Table 1. Comparison of linear crack sizing between microscopy observation and ultrasonic inspection.

		Microscopy		UT
Sample	Crack #	Length (mm)	Opening (µm)	Length (mm)
P3	1	1.2	3	1
P3	2	1.4	9	1.2
P4	5	1.5	2	1.3
P6	10	1	2	0.8
P6	9	1.2	2	1

The image morphology is also investigated on some complex cracks. An image is shown in Fig. FIG 6. The ultrasonic image is presented and compared with a PT image (observed with low magnification microscopy after cleaning, in insert). The sizing and the morphology of the cracks was well fitted between the two images. The high magnification visualization of the cracks allows us to measure the opening of the cracks at approximately 2 µm.

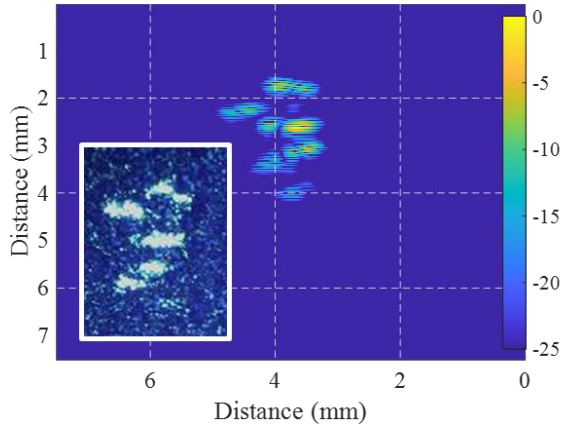

FIG 6. PWI acquisition. Illustration of the comparison of images obtained on complex cracks from ultrasonic and microscopy visualization (insert). Images highlighted complex cracks of similar morphology and size. UT image is in dB scale.

3.2 Imaging of corrosion pitting

Detection of corrosion pitting is a subject of significant interest in surface inspection. We address this point by simulating corrosion pitting using HFB holes at the surface of steel plate parts. The theoretical diameter and the depth of the different holes are given in Table **Erreur ! Source du renvoi introuvable.**. They range from 100 µm to 300 µm in diameter and 100 µm to 500 µm in depth. A reference characterization has been performed after drilling and the diameter and depth of the different holes correspond to the theoretical ones with an error of 20 µm. The holes are aligned on two imaginary lines separated by 10 mm. Each hole is also separated by 10 mm from its neighbor on a given line. Imaging all the holes from one acquisition is thus quite challenging, as it requires a good spatial definition while a large area is imaged. We experimentally found that a ROI zone of 50×15 mm, with a pixel size of 40 µm allows imaging of the holes with a good definition, while retaining good real-time frequency imaging (few hertz).

Table 2. Theoretical dimensions of the different HFB holes imaged in Fig. 7

		a	b	c	d	e	f	g	h
Ref	Diameter (mm)	0.2	0.2	0.2	0.3	0.1	0.1	0.1	0.3
	Depth (mm)	0.1	0.3	0.5	0.3	0.1	0.2	0.3	0.15
UT	Diameter (mm)	0.2	0.28	0.36	0.36	0.28	0.32	0.32	0.4
	Depth (mm)	*s*	*d*	*d*	*d*	*s*	*s*	*d*	*s*

An experimental acquisition is illustrated in Fig. 7. Here we used a FMC acquisition scheme. The holes are imaged on the right part of the image. They have a point-like shape, which is a signature of their small size with respect to the image area. We also observe a linear signal around 26 mm, which is related to a parasitic echo in the rexolite wedge. On the left we plot the amplitude of the signal for imaginary lines passing through the middle of the holes.

We attempted a hole sizing from the plots, first, considering the FWHM of each hole to evaluate its diameter. The correspondence with the real size of the holes is modest as UT sizing tends to oversize the hole's diameter by comparison to the reference evaluation. This could be related to the choice of the FWHM criterion but also to the pixel size of the image, 0.04 mm, which is maybe too large in comparison to some hole diameters (especially for diameter < 200 µm). Second, the amplitude of the signal can be used to estimate the hole depth. Indeed, in that case, the wavelength of the Rayleigh wave is 200 µm and approximately 90% of the energy of the Rayleigh wave is confined in a depth of about one wavelength. In that case, the reflection coefficient is maximal. For holes with a depth smaller

than 200 µm, part of the energy of the Rayleigh wave passes down the holes. The reflection coefficient is reduced. We arbitrarily propose to fix a threshold at −2 dB from the maximum and, depending to the amplitude of the signal, to class the hole as deep (depth > 200 µm, amplitude of the signal larger than −2 dB, *d* symbol in Table 2) or shallow (depth ≤ 200 µm, amplitude of the signal smaller than −2 dB, *s* symbol in Table 2). This criterion allows us to find a good correlation between measurements.

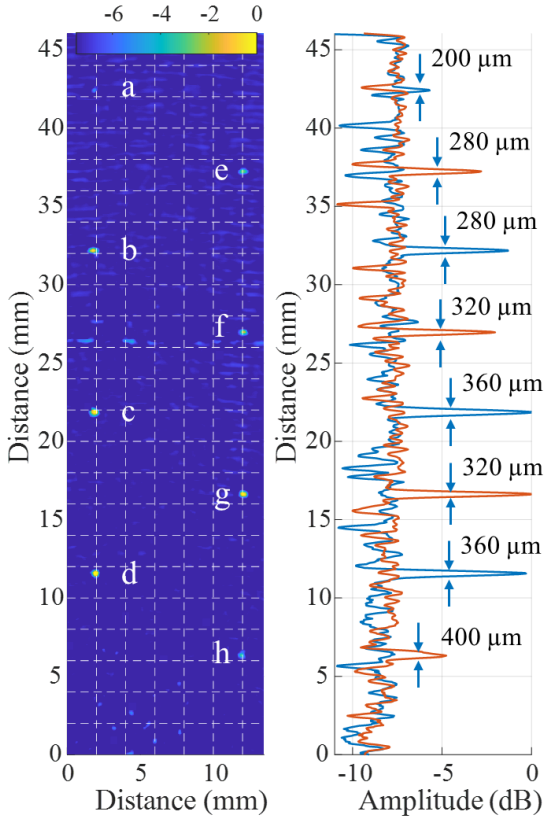

FIG 7. FMC acquisition. Left: T-scan (dB scale) of holes. The signal at ~ 26 mm is related to a parasitic echo in the rexolite wedge. Right: Intensity of the signal on two imaginary lines passing through the holes. Two lines are used to size the HFB.

3.3 Imaging of corrosion pitting under a protective coating

Some surfaces can be protected from corrosion by applying a protective coating. Here we investigate a steel plate (same material as in Section 3.2) covered by 20 µm of cadmium.

Cadmium is a classic anticorrosion coating, compatible with the European REACH norm. HFB holes are drilled after application of the coating.

Before further experiments were undertaken, an evaluation of the impact of the cadmium layer on the surface wave velocity (in comparison to Rayleigh wave velocity in steel) was carried out using CIVA software (Guided wave module, see Supplementary Materials). The energy velocity is computed at 15 MHz for a monolithic steel part (5 mm thick) and a bilayer of the same steel covered by a thin layer of cadmium. Adding a cadmium layer of 20 µm reduces the energy velocity of the surface wave from ~3000 m/s to 2700 m/s. The impact of the cadmium layer is thus considerable and must be taken into account. However, the elastic properties of the cadmium layer are not perfectly known. Next an experimental evaluation of the surface wave velocity is performed. This is done by considering the distance between two neighboring holes equal to 10 mm. Finally we calculate a wave velocity of 2750 m/s instead of 3080 m/s on the monolithic part.

An image of the inspection of such sample is shown in Fig. **Erreur ! Source du renvoi introuvable.**. First note that the signal is noisier than for the monolithic part evaluation. This could be attributed to more energy losses in the multilayer configuration compared to the monolithic one. Second, we also observed some blurring of the holes farthest from the probe. This effect is attributed to a velocity dispersion effect caused by thickness variations of the cadmium layer along the wave propagation. A demonstration is proposed in the Supplementary Material by imaging the four aligned holes from both the “down” and “up” directions. The farthest holes from the probe are shown to be consistently the most blurred (see Supplementary Materials) because of velocity variations not taken into account in the image synthesis. Such effects prevent determination of a correct sizing of the different holes and hole size evaluation can only be done in the first 10 mm in front of the probe in such a bilayer configuration.

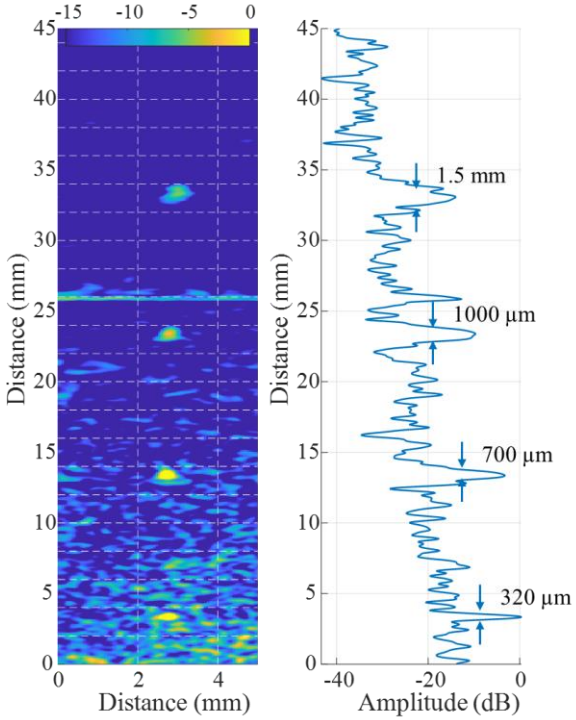

FIG 7. PWI acquisition. Left: T-scan (dB scale) image of holes. The signal at ~26 mm is related to a parasitic echo in the rexolite wedge. Right: Intensity of the signal on an imaginary line passing through the aligned holes. Line is used to size the HFB.

3.4 Freckles imaging

Segregations are the enrichment of atoms, ions, or molecules in a microscopic region of a materials system, typically an alloy. Freckles are macro size segregations that can appear during the solidification process. These defects have a negative influence on high temperature mechanical properties of alloys and can reduce the life of a metallic part. They can virtually only be detected using macrography or eddy currents. However, such methods present various limitations, and this makes their detection difficult.

However, segregations can be damaging for the metallic part because they locally modify the mechanical properties of the material by an overconcentration of some chemical elements. That local variation can lead to an interface for an incoming elastic wave. Rayleigh

waves propagate with an elliptic polarization in the sagittal plane, i.e., with a longitudinal and a transverse polarization in the plane normal to the surface. Moreover, the imaging method requires us to consider either cylindrical waves or plane waves propagating in different directions. Thus, the probability is strong, when the PA is placed in front of a freckle, for the incoming wave to be close to an optimal configuration for freckle detection, where a significant part of the wave is reflected at the interface. So, the method seems interesting for imaging surface segregation.

We consider here a freckle that is at the surface of a nickel-based alloy. It has been previously imaged by both eddy currents and macrography. The ultrasonic image of the freckle is shown in Fig. 8. On that image, the freckle signal presents a rather good signal to noise ratio, between 5 and 10 dB above the surface signal. Moreover, the ultrasonic sizing of the freckle is in good agreement with the macrographic one. We also observe around the freckle a signal reduction, which we cannot currently explain. Such an effect is, however, interesting as it could be used as a marker of freckle detection (instead of other surface indications) if such an effect is confirmed from more systematic investigations and observed only for freckles or segregations.

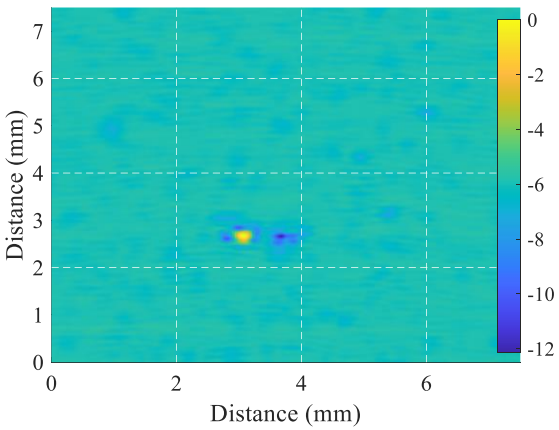

FIG 8. FMC acquisition. T-scan imaging of an emerging segregation (freckle) on a metallic alloy. Image is in dB scale.

4. Imaging with complex geometries

Some inspected surfaces are plane and far from singularities such as edges, while others involve more complexity, such as curvature or proximity to edges or discontinuities. NDT inspection of such surfaces is even more important as such locations are often the places of stress concentration and may be the preferred site for cracks to start or accelerated aging. For instance, pipelines are curved parts with elbows or rivet holes that serve as stress risers and require particular attention. Unfortunately, many methods do not allow inspection of these surfaces and the choice quickly becomes more restricted than for large plane surfaces.

We now address the effectiveness of the Rayleigh surface imaging method with complex surface geometries. First, we will look at discontinuities near an edge and then inspection of curved cylindrical, parts.

4.1 Imaging close to an edge

Surface imaging close to edges is difficult. Indeed, electromagnetic methods fail because of the dissymmetry in the electric field induced by the space dissymmetry. Most of the thermal methods have similar problems and even optical inspections can be significantly affected.

We first investigate the method performances for imaging defects close to sharp edges. We consider for that work a series of HFB holes similar to those described in Section 3.2, drilled in very close proximity to a sharp edge on the metallic part. The shortest distance from edge to hole is 100 µm and the edge has a linear profile. To perform the inspection, the PA is placed parallel to the edge and a few mm in front of it. Experiment is schemed on Fig. 10. The corresponding T-scan image of the surface is shown in Fig. 10, with a pixel size of 0.04 mm.

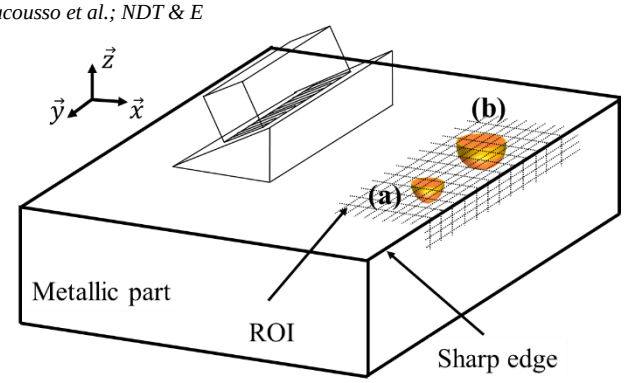

FIG. 9 : Scheme of experiments performed for imaging holes close to an edge. The shortest distance from holes to edge is 100 µm. The ROI zone is on either side of the edge.

In Fig. 10, the linear signal at around 2.5 mm on the *y*-axis corresponds to the reflected echo from the linear edge. A few tens of microns before this there are two small echoes, indicated by large arrays and spaced by 10 mm. They correspond to the reflection of the elastic signal of the HBF holes, labeled (a) and (b). Their diameters and depths are 0.2 mm and 0.1 mm for hole (a) and 0.3 mm and 0.15 mm for hole (b), respectively.

A UT sizing is proposed from the detected image. First, the signal between the dotted lines parallel to the *x*-axis is summed and plot above the echo signal (continuous line). The FWHM of the signal from the holes allows sizing diameters of hole (a) at 0.44 mm and hole (b) at 0.56 mm. The overestimation of the UT sizing could be related to parasitic echoes between the sharp edge and the hole, which could increase the image signal. Note the amplitude of the hole (b) is larger than the amplitude of hole (a), which is in good agreement with the depths of the holes. Second, we consider the signal summed between the vertical dotted lines for each plot. The initial calculation contained a strong contribution from the reflection on the edge, which is suppressed by subtracting the mean signal along the *y*-axis of the whole image. The obtained signals for (a) and (b) holes are plotted on Fig. FIG 10 and are

used to indicate the diameters of the holes at 0.16 mm and 0.28 mm, respectively. Such sizing is in good agreement with the real size of the holes.

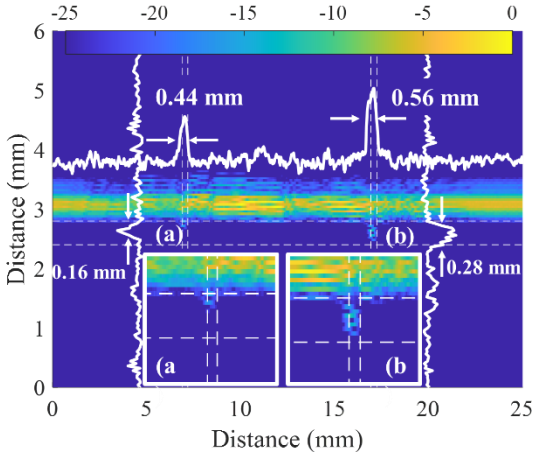

FIG 10. PWI acquisition. T-scan image of a surface close to a sharp edge. The continuous lines correspond to the mean signal between the dotted lines. They are used to find the diameter of the holes. Inserts are zooms of holes. Images are in dB scale.

We finally image a hole close to the right angle formed by two sharp edges on a metallic part. The smallest distance between the hole circumference and the edges of the sample is 100 µm. Experiments is schemed on Fig. 11.

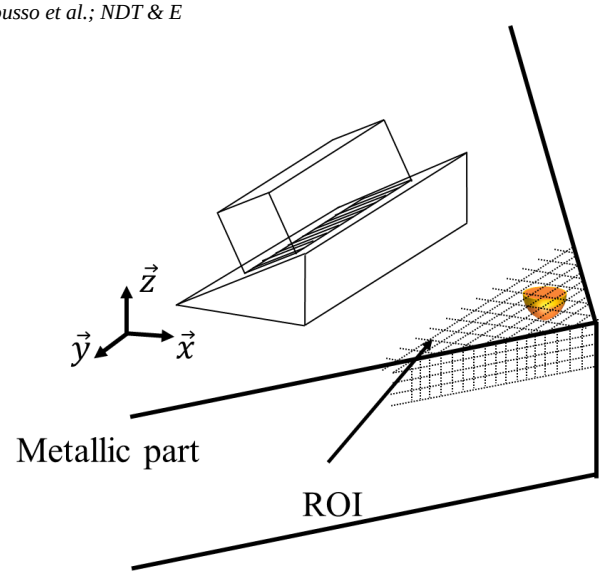

FIG. 11 : Scheme of experiments performed for imaging holes close to an angle. The shortest distance from hole to edge is 100 µm. The ROI zone is on either side of the angle.

The T-scan image is presented on Fig. FIG 14. The two crossing lines are the edges of the metallic part. The inspected area is defined by the zone down these lines. The hole is detected but seems oblong. We plot the intensity signal of imaginary lines passing through the center of the hole, along the *x*- and *y*- directions. The corresponding FWHM sizing is 0.55 mm along the *x*-axis and 0.225 mm along the *y*-axis. Again, such dissymmetry is attributed to parasitic multiple reflection which could appear between the edges of the metallic part and the holes and could lead to artifacts.

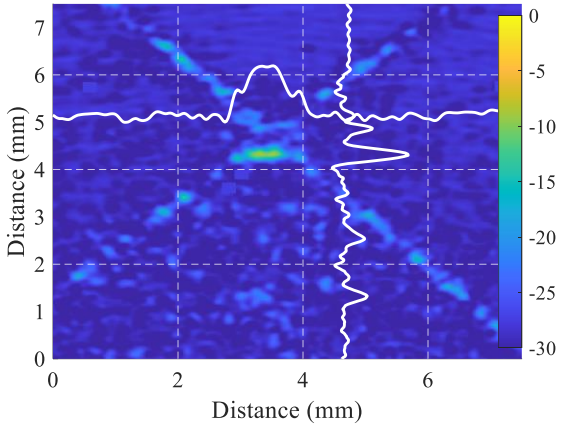

FIG 12. FMC acquisition. T-scan image of a surface close to a sharp angle. The continuous lines correspond to the signal of a continuous imaginary line passing through the hole. Image is in dB scale.

4.2 Surface imaging of a curved edge

One other limit of current surface inspection methods is in imaging around curved edges, even if the edge is smooth with a few mm of curvature. We consider here a metallic sample, which present a smooth edge, with a curvature of 5 mm radius. A crack with a micrometric sized opening is in the curvature, parallel to the edge. Such a sample is used to demonstrate the Rayleigh wave imaging capability in a curved surface. The PA is placed at the surface of the sample, a few centimeters from the edge. The PA is parallel to the edge and the pixel size is 25 µm. A schematic of the experiment is shown in FIG 13. The crack is in the ROI zone, which is symbolized by the grid of dotted lines. The T-scan image of the cracks is shown in FIG 14. A PT visualization is also presented in the insert. A good qualitative correspondence is obtained.

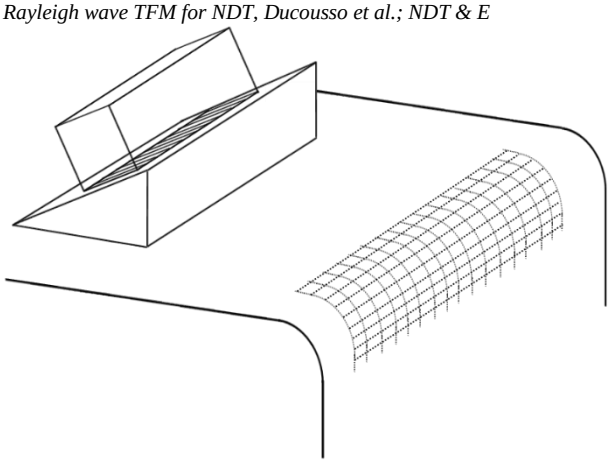

FIG 13. Schematic of experiments for imaging the surface in a curve edge. The ROI is symbolized by the dotted grid. The emerging crack is in the ROI.

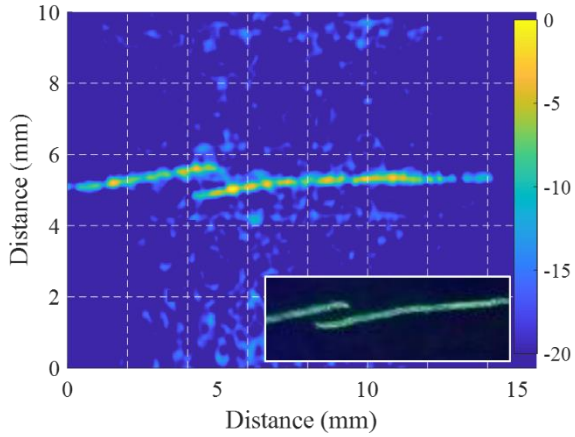

FIG 14. PWI sequence. T-scan image of cracks in a curve edge. An image obtained from PT is presented in insert. A good agreement between the two images is obtained. UT image is in dB scale.

4.3 Surface imaging after an angle

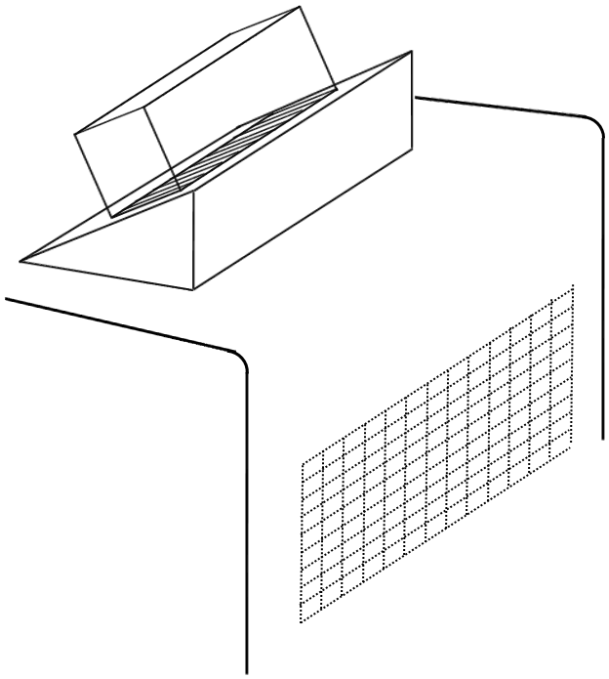

FIG 15. Schematic of experiments for imaging a surface after an edge. The dotted grid symbolizes the ROI, which contain the emerging crack.

Some surfaces are complex to image because of difficult access, for example, because of angles which prevent a direct access to the surface for an optical or magnetic inspection and so a long distance approach is required. Considering a PA of 15 mm and 21 mm of active aperture, the far field limit for a Rayleigh wave, which propagates at 3000 m/s, is more than 500 mm. This makes the Rayleigh inspection suitable for a long distance remote inspection, which is of significant interest for surfaces with complex access. We demonstrate this by imaging a crack on a surface that is after an angle (1 mm radius curvature). The PA and the cracks are thus on the same surface but there is an angle of 90° between them. Figure 15 illustrates such a configuration, with the cracks in the ROI zone. The angle can lead to a reflection of the Rayleigh wave but if the angle is not in the ROI, such a signal is not imaged. In this case, the imaged crack is shown in FIG 16. A PT visualization is also presented in the

insert. The signal is lower, probably because of a partial reflection of the Rayleigh wave at the surface edge, but crack is well detected and fits with the PT inspection.

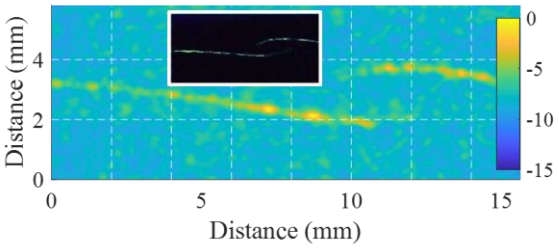

FIG 16. FMC sequence. T-scan image of cracks after an edge. An image obtained from PT is presented in the insert. A good agreement between the two images is obtained. UT image is in dB scale.

4.4 Tube surface imaging

Finally, we demonstrate the suitability of Rayleigh wave inspection for curved surfaces by imaging FBH holes on a steel tube. The tube has a radius of 40 mm and is 5 mm thick. For this inspection, a specific wedge for the PA has been designed, with a curved surface, the same radius as the exterior of the tube to allows a good coupling. The angle between the incident wave and the tangent of the tube at the emerging point is equal to θ^w. The wedge allows us to generate a Rayleigh wave at the surface of the tube. The schematic of the experiment is shown in FIG 17.

Different FBH holes are drilled on the tube's exterior surface. They have a diameter from 0.1 to 0.3 mm and the same depth, as shown in FIG 17. They are contained in the ROI zone for surface wave imaging. The obtained image is shown in Fig. 18. The signal to noise ratio is reduced in comparison to Fig. 7, probably because of a worse coupling than in the plane configuration. Nevertheless, holes are well detected and a sizing is proposed. The intensity of the signal from the holes is plotted on the right and sizing from FWHM is

quantified. We found a good agreement using the same procedure for depth evaluation as in Section 3.2 in the plane case.

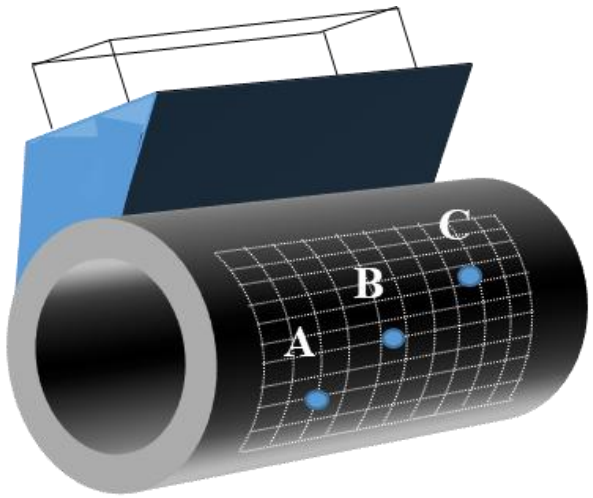

FIG 17. Scheme of experiments for imaging an exterior surface of a metallic tube. The dotted grid symbolizes the ROI. HBF holes are in the dotted grid. Holes have the same diameter and depth: 0.1 mm for hole A, 0.2 mm for hole B, 0.3 mm for hole C.

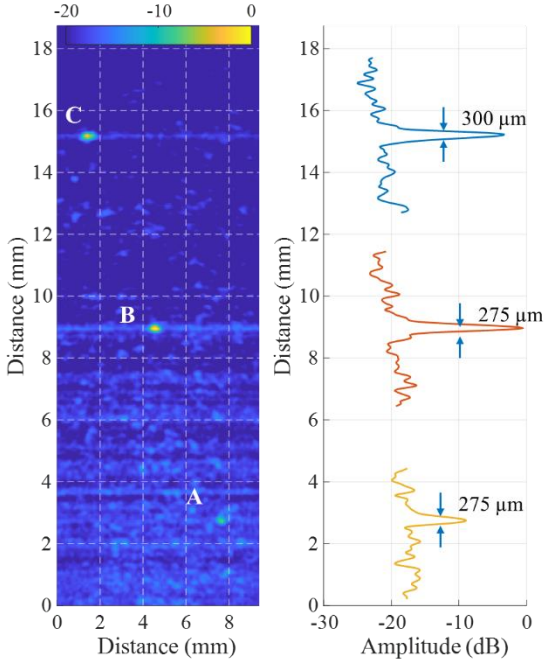

FIG 18. PWI acquisition. Left: T-scan image of the exterior surface of a tube. Micrometric FBH are imaged. Right: Intensity of the signal on an imaginary line passing through the different holes.

5. Conclusion

We highlighted in the article a new, efficient method for surface inspection based on using surface waves combined with synthetic focusing algorithms for TFM. First, we demonstrated the method is efficient for imaging and sizing several surface defects such as cracks, micro size holes, or segregations, on large surfaces. This illustrates the high sensitivity of the method for indications that are difficult to detect, such as segregations, and the capacity to detect defects as small as 100 µm. We then applied the method for a range of different geometrical complexities, from proximity to edges or angles, to circular surfaces. Surface imaging using Rayleigh waves combined with TFM is thus a very efficient method that can be applied for several NDT needs. In addition to its good sensitivity performance and

adaptability to many geometries, the method is free of chemical preparation and cleaning. Moreover, this method can be fully automated, from acquisition to decision, making it compatible with digitalization and surface digital twins for Industry 4.0.

6. Declaration of competing interest

The authors declare that they have no known competing financial interests or personal relationships that could have appeared to influence the work reported in this paper.

7. Acknowledgements

Authors would like to acknowledge Frederic Jenson and Benoît Lasjaunias, for helpful discussions about image synthesis and comparison. They also would like to acknowledge CEA, especially Stéphane Leberre and his team for helpful documentation on imaging algorithms proposed in CIVA software and Karim Jezzine for helpful discussions about surface waves behavior on bilayers.

Author contributions

Funding

This research did not receive any specific grant from funding agencies in the public, commercial, or not-for-profit sectors.

8. Bibliography

[1] S. Burke and R. Ditchburn, "Review of Literature on Probability of Detection for Magnetic Particle Nondestructive Testing," *Maritime Platforms Division, DSTO Defence Science and Technology Organisation,* 2013.

[2] T. Li, D. Almond and A. Rees, "Crack imaging by scanning pulsed laser spot thermography," *NDT&E International,* vol. 44, pp. 216-225, 2011.

[3] S. E. Burrows, S. Dixon, S. Pickering, T. Li and D. Almond, "Thermographic detection of surface breaking defects using a scanning laser source," *NDT & E International,* vol. 44, pp. 589-596, 2011.

[4] S. Ahmadi, P. Burgholzer, P. Jung, G. Caire and M. Ziegler, "Super resolution laser line scanning thermography," *Optics and Lasers in Engineering,* vol. 134, p. 106279, 2020.

[5] M. Pan, Y. He, G. Tian, D. Chen and F. Luo, "Defect characterisation using pulsed eddy current thermography under transmission mode and NDT applications," *NDT&E Internationa,* vol. 52, pp. 28-36, 2012.

[6] B. Drinkwater and P. Wilcox, "Ultrasonic arrays for non-destructive evaluation: A review," *NDT&E International,* vol. 39, pp. 525-541, 2006.

[7] J.-G. Minonzio, M. Talmant and P. Laugier, "Guided wave phase velocity measurement using multi-emitter and multi-receiver arrays in the axial transmission configuration," *The Journal of the Acoustical Society of America,* vol. 127, pp. 2913-2919, 2010.

[8] M. Ducousso, A. Dalodière and A. Baillard, "Evaluation of the thermal aging of aeronautical composite materials using Lamb waves," *Ultrasonics,* vol. 94, pp. 174-182, 2019.

[9] C. Holmes, B. Drinkwater and P. Wilcox, "Post-processing of the full matrix of ultrasonic transmit–receive array data for non-destructive evaluation," *NDT&E International,* vol. 38, pp. 701-711, 2005.

[10] L. Le Jeune, S. Robert, E. Lopez Villaverde and C. Prada, "Plane Wave Imaging for Ultrasonic Non-Destructive Testing: Generalization to Multimodal Imaging," *Ultrasonics,* vol. 64, pp. 128-138, 2016.

[11] J. Camacho, M. Parrilla and C. Fritsch, "Phase Coherence Imaging," *IEEE Transactions on Ultrasonics, Ferroelectrics, and Frequency Control,* vol. 56, pp. 958-974, 2009.

[12] J. Cruza, J. Camacho and C. Fritsch, "Plane-wave phase-coherence imaging for NDE," *NDT & E International*, vol. 87, pp. 31-37, 2017.

[13] G. Matrone, A. Ramalli, J. D'hooge, P. Tortoli and G. Magenes, "A Comparison of Coherence-Based Beamforming Techniques in High-Frame-Rate Ultrasound Imaging With Multi-Line Transmission," *IEEE Transactions on Ultrasonics, Ferroelectrics, and Frequency Control*, vol. 67, no. 2, pp. {329-340, 2020.

[14] M. Ducousso and F. Reverdy, "Real-time imaging of microcracks on metallic surface using total focusing method and plane wave imaging with Rayleigh waves," *NDT & E International*, vol. 116, p. 102311, 2020.

[15] Extende, "CIVA 2023 : Release note," *https://www.extende.com/files/extende/download_files/CIVA_2023_Release_Note_EN.pdf*.

[16] J. Camacho, C. Fritsch, J. Fernandez-Cruza and M. Parrilla, "Phase Coherence Imaging: Principles, applications and current developments," *Proc. Mtgs. Acoust.* , vol. 38, p. 055012, 2019.

[17] Z. Wang, A. Bovik, H. Sheikh and E. P. Simoncelli, "Image quality assessment: from error visibility to structural similarity," *IEEE Transactions on Image Processing*, vol. 13, pp. 600-612, 2004.